



Cite this: DOI: 10.1039/c9nr07683b

Tunable plasmonic HfN nanoparticles and arrays†

 Sven H. C. Askes, ^a Nick J. Schilder, ^a Erwin Zoethout, ^b Albert Polman ^a
and Erik C. Garnett ^{*,a}

We present the fabrication of tunable plasmonic hafnium nitride (HfN) nanoparticles. HfN is a metallic refractory material with the potential of supporting plasmon resonances in the visible range, similar to silver and gold, but with the additional benefits of high melting point, chemical stability, and mechanical hardness. However, the preparation of HfN nanoparticles and the experimental demonstration of their plasmonic potential are still in their infancy. Here, high quality HfN thin films were fabricated, for which ellipsometry shows their plasmonic potential. From these thin films, nanorods and nanotriangles were milled using a focused ion beam and the plasmon resonances were identified using cathodoluminescence mapping. As an alternative fabrication strategy, an optimized electron-beam lithography procedure was used to prepare arrays of HfN nanoparticles, which also exhibited clear surface plasmon resonances. These results pave the way to further explore HfN nanoparticles in plasmonically-powered applications where materials robustness is essential.

 Received 5th September 2019,
Accepted 7th October 2019

DOI: 10.1039/c9nr07683b

rsc.li/nanoscale

Introduction

Noble metal plasmonic nanostructures feature extraordinary visible light absorption cross sections, highly tunable optical responses, and capability of enhancing the local energy density of light in subwavelength volumes. Unconventional plasmonic materials such as the group-4 metal nitrides (TiN, ZrN, and HfN) have recently attracted strong research interest^{1–3} for complementing the use of Au/Ag in plasmonic applications at high temperature and high photon flux, because of two main reasons: (i) their optical behavior is similar to Ag and Au but is more tunable by varying the material stoichiometry, and (ii) their refractory material properties bless them with extremely high melting points [$T_m(\text{HfN}) = 3583 \text{ K}$],⁴ excellent chemical stability, and mechanical hardness. Thus, metal nitride nanoparticles are expected to have more stable and reliable optical properties at demanding operating conditions than their noble metal counterparts. Plasmonic nanostructures are also well studied for their ability to generate highly energetic, “hot” electrons upon optical excitation, which can be extracted for driving a wide variety of chemical reactions.^{5–7} In this context, especially HfN is a promising material because the large phonon bandgap leads

to a significantly slower hot electron–phonon relaxation pathway ($\tau \approx 1\text{--}3 \text{ ns}$)^{8,9} compared to the noble metals ($\tau \leq 3 \text{ ps}$).¹⁰ This in turn may lead to higher extraction efficiencies and the ability to drive kinetically slower chemical reactions before charge-recombination occurs.⁵

Although there are various reports on plasmonic TiN and ZrN nanoparticles,^{11,12,13–20,21} detailed reports on the fabrication of plasmonic HfN nanoparticles are currently very scarce,²² with no method reported for controlling particle shape or size. Furthermore, the evidence of their plasmonic properties so far consists of ensemble measurements of the localized surface plasmon resonance (LSPR) using absorption spectroscopy. However, since many plasmonic applications rely on shape and size control to tune the resonance frequency and spatial distribution of LSPRs, it is crucial to characterize this spatial variation in both individual nanoparticles and in uniform arrays. This motivated us to explore and develop lithographic preparations for obtaining plasmonic HfN nanostructures and spatially mapping their LSPRs using cathodoluminescence (CL) spectroscopy.

We realized that such a task is non-trivial, because although the refractory material properties are a blessing in the eventual plasmonic applications, they are an inconvenience for the preparation of nanoparticles with lithography.^{1,23} On the one hand, due to the high melting point and binary atomic nature, it is challenging to deposit stoichiometric HfN using thermal or e-beam evaporation and without loss of nitrogen. The usual deposition technique for obtaining high-quality HfN thin films is therefore reactive sputter coating,²⁴ which uses a Hf target and a nitrogen-containing plasma (Fig. S1†). However,

^aCenter for Nanophotonics, AMOLF, Science Park 104, 1098 XG Amsterdam, The Netherlands. E-mail: e.garnett@amolf.nl

^bDutch Institute for Fundamental Energy Research (DIFFER), De Zaaie 20, 5612 AJ Eindhoven, The Netherlands

†Electronic supplementary information (ESI) available. See DOI: 10.1039/c9nr07683b

this technique is incompatible with standard positive-tone resist lithography due to the hostile presence of the reactive plasma and the often required high temperatures during deposition. Another cumbersome disadvantage is the poor directionality of the sputter source, which leads to challenges in the achievable particle resolution and height. On the other hand, negative-tone resist strategies are severely limited by the high chemical inertness, which prevents effectiveness of chemical and reactive ion etching techniques.

In short, before the beneficial material properties of HfN can be fully exploited in plasmonic applications, it is crucial to develop fabrication techniques and experimentally examine the achievable properties of LSPRs in such fabricated particles. In this work, we prepare high quality HfN films with tunable properties using reactive sputtering. We then show that both focused ion beam milling and electron beam lithography can be used to make individual nanoparticles and uniform arrays with controlled shape and size. Finally, we use CL spectroscopy to map the LSPRs in particles with different shapes and sizes.

Results and discussion

In order to obtain high-quality plasmonic HfN nanoparticles we first optimized the deposition of HfN by reactive sputter coating. By varying the nitrogen partial pressure in the sputter plasma, a full range of silver-colored to golden to brown HfN thin layers was obtained on both Si(100) and c-plane sapphire substrates (Fig. 1a) without active substrate heating. Extraction of the optical constants (permittivity ϵ' and ϵ'') by spectroscopic ellipsometry allowed us to select growth conditions for optimal plasmonic performance in the visible-NIR region, *i.e.* for which the plasmonic quality factor $Q_{\text{LSPR}} = -\epsilon'/\epsilon''$ was maximized (Fig. S2,† optimized result in Fig. 1c). In such conditions, a lustrous silver-golden material was obtained (Fig. 1a, indicated with “HfN”), for which the optical constants could be well described by the classical free-electron (Drude) model with unscreened plasma frequency $\hbar\omega_p = 8.19$ eV, damping constant $\hbar\gamma = 0.48$ eV, and high-frequency limit $\epsilon_\infty = 4.62$ eV (Fig. S3†), very similar to literature values on metal-like HfN.^{1,25,26} A screened bulk plasmon resonance at $\lambda \sim 370$ nm (≈ 3.35 eV) was observed (for $\epsilon' = 0$), while the bulk plasma frequency is expected at much higher energy, which has been attributed before to the presence of interband transitions with a threshold at near-UV frequencies.²⁵ The UV-Vis absorption spectrum indeed showed typical noble metal behavior with an increase in reflection towards infrared wavelengths, while the absorption increased towards the UV as the result of the interband transitions (Fig. S4†).

The Hf:N stoichiometry was determined to be 1:0.96 using 2 MeV He Rutherford Backscattering Spectrometry (RBS, Fig. 1d), with uniformity throughout the entire film and less than 2 atom% oxygen in the material bulk (see measurements on carbon substrate in Fig. S6†). Cross-correlating the RBS-derived stoichiometry and the extracted optical constants for HfN deposited at elevated nitrogen partial pressures revealed

that the plasmonic performance greatly diminished upon deviating from 1:1 stoichiometry (Fig. S2 and Fig. S5†). X-ray Photoemission Spectroscopy (XPS, Fig. 1e) and depth profiling (Fig. S9†) confirmed (i) Hf and N binding energies matching literature spectra of HfN,^{29,30} (ii) 1:1 stoichiometry with excellent uniformity, and (iii) excellent purity with negligible amount of incorporated oxygen and carbon in the material bulk.

The material was further characterized by X-ray diffraction (XRD), Atomic Force Microscopy (AFM), and Raman spectroscopy. XRD showed that HfN was deposited single-phased with preferred (100) crystal orientation on both Si(100) and c-plane sapphire with an average crystallite size of 40–47 nm and a cubic lattice constant of 4.53 Å (Fig. 1f and Fig. S8†).²⁷ A cross-cut of the film was visualized using Scanning Electron Microscopy (SEM), revealing that the crystallites grow in a columnar fashion (Fig. 1b), similar to reports on other transition metal nitrides.^{1,31,32} Despite polycrystallinity, AFM revealed that the surface was very smooth (0.3 nm root-mean square roughness, Fig. S7†). The Raman spectrum (Fig. 1g) consisted of a first-order acoustic band (<200 cm⁻¹), first-order optical band (520 cm⁻¹) and several second-order combinations,²⁸ which confirmed the wide phonon bandgap reported for this material due to the large atomic mass difference ($m_{\text{Hf}}:m_{\text{N}} = 178:14$). Finally, 4-point probe electrical resistance measurements identified a low sheet resistance of 2.7 Ω per sq. (66 μΩ cm bulk resistance), in line with literature values.^{1,24} Overall these data demonstrate that high-quality metallic HfN was obtained with suitable physical-optical properties for making plasmonic nanoparticles.

We fabricated HfN nanoparticles with various sizes and shapes using FIB milling of a 70 nm HfN thin film and mapped the plasmon resonances using a focused 30 keV electron beam as an optical excitation in a CL-SEM setup (Fig. 2). In total 10 differently-sized nanorods and nanotriangles were prepared (SEM in Fig. S11†) and Energy Dispersive X-ray Spectroscopy (EDS) mapping confirmed that the particles consisted of HfN (Fig. 2b and Fig. S10†). The nanostructure dimensions were chosen to roughly match the attainable size of structures fabricated by e-beam lithography, discussed later in this work. Finite Difference Time Domain (FDTD) simulations predicted that such relatively large structures mainly resonate at near-infrared wavelengths with broad tailing towards the visible light region, partially due to relatively high losses in the material (Fig. S12†). For both 295 × 95 nm and 485 × 75 nm nanorods, at resonance conditions the extinction is expected to be dominated by absorption (absorption $\approx 60\%$ of total extinction cross section, Fig. S12b/c†), while for a 415 nm equilateral nanotriangle it is dominated by scatter (absorption $\approx 35\%$ of total extinction cross section, Fig. S12d†). As expected, for nanorods the simulations exhibit a rather weak plasmon resonance for source polarization along the short axis (around 500 nm) and a much stronger plasmon resonance along the long axis at near infrared wavelengths (>1000 nm). CL was used in the coherent mode in which the time-varying electric field of an electron polarizes the nano-

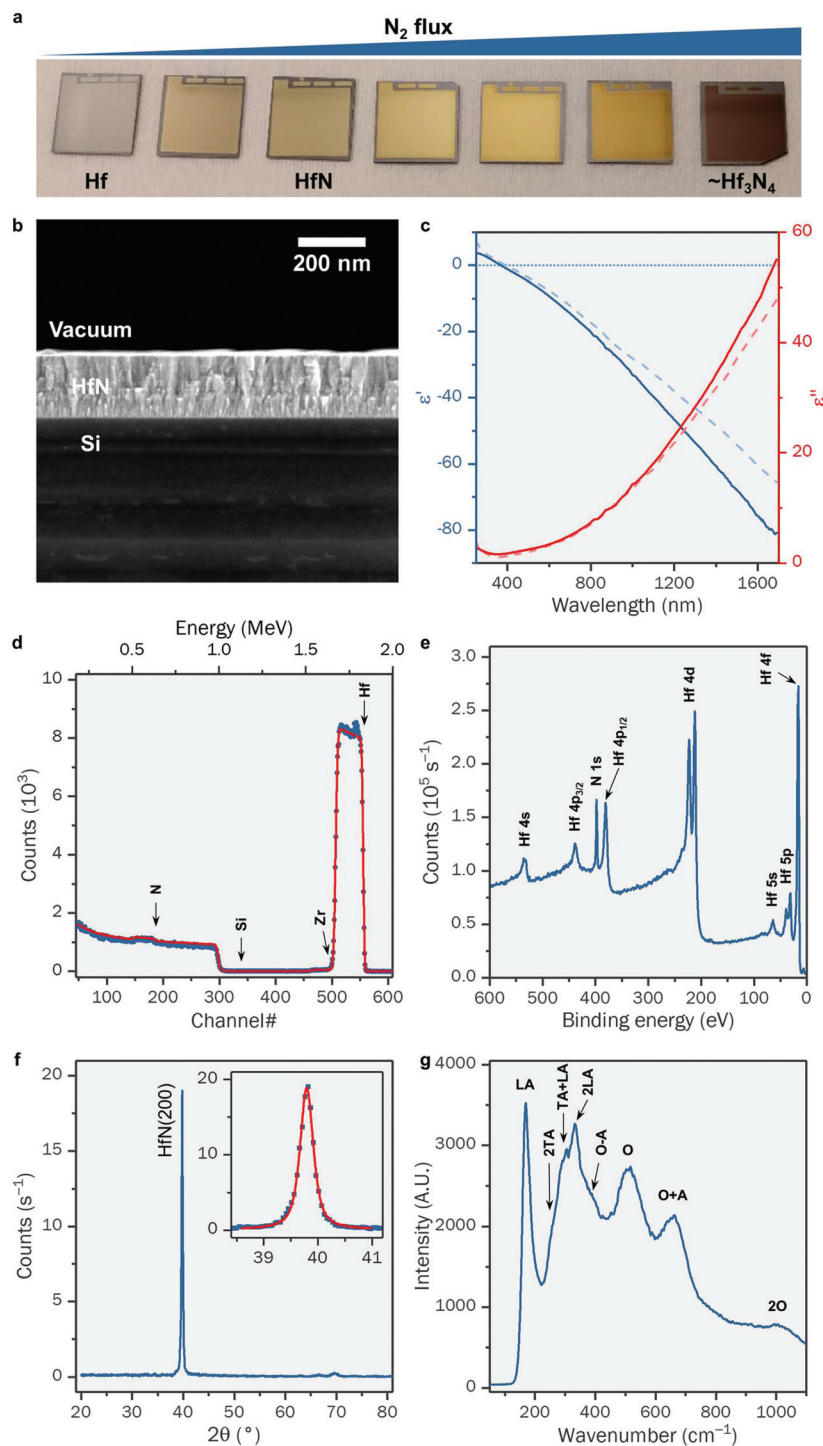


Fig. 1 Characterization of an optimized HfN thin film grown by reactive sputter coating. (a) Photograph of 200 nm HfN_y ($0 \leq y \leq 1.33$) layers deposited by reactive sputter coating on 12×12 mm Si substrates. (b) SEM cross section of a 200 nm HfN thin film on crystalline Si(100). (c) Real (solid blue curve, left) and imaginary (solid red curve, right axis) parts of the dielectric constant obtained from spectroscopic ellipsometry measurements of a 200 nm-thin HfN film. Dashed curves indicate the data compiled by Ribbing and Roos.²⁶ (d) RBS spectrum of HfN thin film on Si. Fit to the data (red) made using SIMNRA software, revealing a Hf : N stoichiometry of 1 : 0.96. Surface channels are indicated per element. (e) XPS spectrum after 500 eV Ar ion erosion to about 35 nm depth (see also Fig. S9†). (f) XRD spectrum of HfN on Si(100). The (200) index corresponds to the reported diffraction pattern of cubic HfN with a lattice constant of 4.53 Å.²⁷ Inset: Pseudo-Voigt-function fit (red, $R^2 = 0.996$) to the HfN(200) diffraction peak, from which a crystallite size of 40 nm was calculated after correction for instrumental broadening. (g) Raman spectrum of HfN on Al_2O_3 thin film. Phonon bands are annotated as previously assigned by Stoehr *et al.*²⁸ A = acoustic, LA = longitudinal acoustic, TA = transverse acoustic, O = optical. The TA peak at 120 cm^{-1} is not visible due to the filter cutoff at $\sim 150 \text{ cm}^{-1}$.

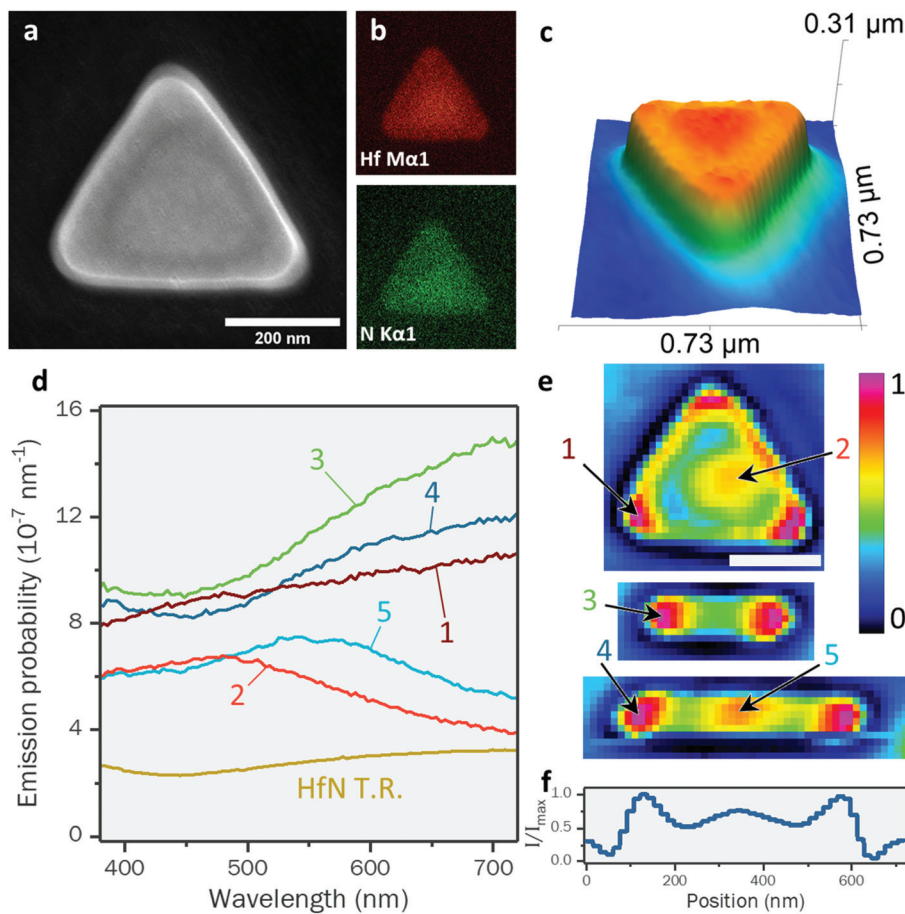


Fig. 2 CL of HfN nanostructures prepared by FIB-milling. (a) SEM micrograph of a 420 nm equilateral HfN nanotriangle. (b) EDX emission map of Hf (top, red) and N (bottom, green) under 5 kV electron impact. (c) AFM 3D reconstruction of the HfN nanotriangle (blue-green-red color scheme added for height discrimination). Note that only the top 70 nm consists of HfN, see Fig. S11.† CL spectra (d) and normalized spectral maps at $\lambda = 500 \pm 50$ nm (e) for HfN triangles and short and long nanorods. The scale bar is 200 nm for all three images. Spectra in panel d correspond to locations arrow-marked in panel e. Transition radiation (T.R.) spectrum of thin film HfN given in yellow. (f) CL intensity at $\lambda = 500 \pm 50$ nm along the long axis of the long nanorod of which the CL map is shown in panel e.

particle that then radiates to the far field creating CL over a broad spectral range.^{33–35} Raster-scanning the electron beam over the nanostructure allows for excitation mapping of LSPR modal distributions. Because CL spectroscopy beyond 1000 nm was challenging due to severe background CL originating from the Si substrate, we instead focused on the 380–720 nm domain, in which we expected to observe higher order plasmonic resonances as previously observed for Ag and Au nanostructures.^{36–39}

The CL maps at $\lambda = 500 \pm 50$ nm for an equilateral 420 nm nanotriangle and two nanorods (295 × 75 and 485 × 75 nm) are presented in Fig. 2e and spectra at selected points are shown in panel d (data for all structures shown in Fig. S13/ Fig. S14†). For all 10 structures the emission intensity is highest at the tips throughout the entire spectrum. The spectral maps for the nanorods are similar to those found earlier for Au and Ag nanorods and are explained by standing plasmon waves along the rod.^{36–39} For both nanorods the high-frequency tail of the first-harmonic resonances are observed at

the tips, increasing in intensity towards the near-infrared (Fig. 2d, spectra #3 and #4). Because the first-harmonic plasmon mode peaks at shorter wavelength for the smaller nanorod, we observe a higher CL-intensity in the visible range for this structure. For the 485 nm rod an antinode is observed in the center (Fig. 2e) corresponding to the second-harmonic resonance which peaks at $\lambda = 550$ nm (Fig. 2d, spectrum #5). The fact that this second-harmonic standing wave is observed at a wavelength very close to the rod length (L) is in agreement with a surface plasmon polariton (SPP) mode index close to 1 ($n_{\text{mode}} = \lambda/L \approx 1.1$ for the second-harmonic)³⁸ that follows from the optical constants in Fig. 1c, and indicates there is only a small phase shift upon SPP reflection off the nanorod ends.⁴⁰ Furthermore, second- and third-harmonics were also observed in larger HfN structures and were consistent with our interpretation of standing wave plasmon-modes (see Fig. S13, S14,† and accompanying discussion). Note that all of the emission spectra are much stronger than the transition radiation of thin-film HfN under the same excitation conditions (T.R., Fig. 2d).

The CL map for the triangular structure shows similar features to that observed for Au triangles in both CL and Electron Energy-Loss Spectroscopy (EELS) using a scanning transmission electron microscope.^{39,41–43} Multiple mode profiles can be observed, due to the spectral overlap of modes. In the CL map at $\lambda = 500 \pm 50$ nm we observe a tip-centered mode with intensity increase towards NIR wavelengths and no observable peaks in the visible range (Fig. 2d, spectrum #1). Notably, for smaller nanotriangles the tip-centered mode shifts to $\lambda = 650$ nm and $\lambda = 500$ nm for 300 nm and 190 nm width, respectively (Fig. S14† spectra #20 and #22). Furthermore, a central mode is observed which peaks at $\lambda = 500$ nm for 420 nm width (Fig. 2d, spectrum #2), blue-shifts to $\lambda = 400$ nm for 300 nm width, and further blue-shifts to UV wavelengths for 190 nm width (Fig. S14† spectra #21 and #23). This is consistent with the blue-shifting of plasmon modes

upon decreasing structural dimensions, as has previously been observed in Au.

Because FIB preparation of HfN nanoparticles that was used above is incompatible with many applications and upscaling, we also explored larger-scale preparation of nanorods and nanotriangles using e-beam lithography on Si and sapphire substrates. A negative-tone resist strategy using hydrogen silsesquioxane (HSQ) and plasma etching of excess HfN with Ar/SF₆ was able to yield nanoparticle arrays (Fig. S15†). However, the nanoparticle edges were rounded and slanted, the z-dimension was limited to <40 nm by the much higher etch-rate of developed HSQ in the plasma etching conditions, and according to EDX the nanoparticle material was implanted with fluorine during etching. We then used a CSAR-62 positive-tone resist in combination with lift-off (Fig. S16†). However, HfN was inevitably only deposited on the

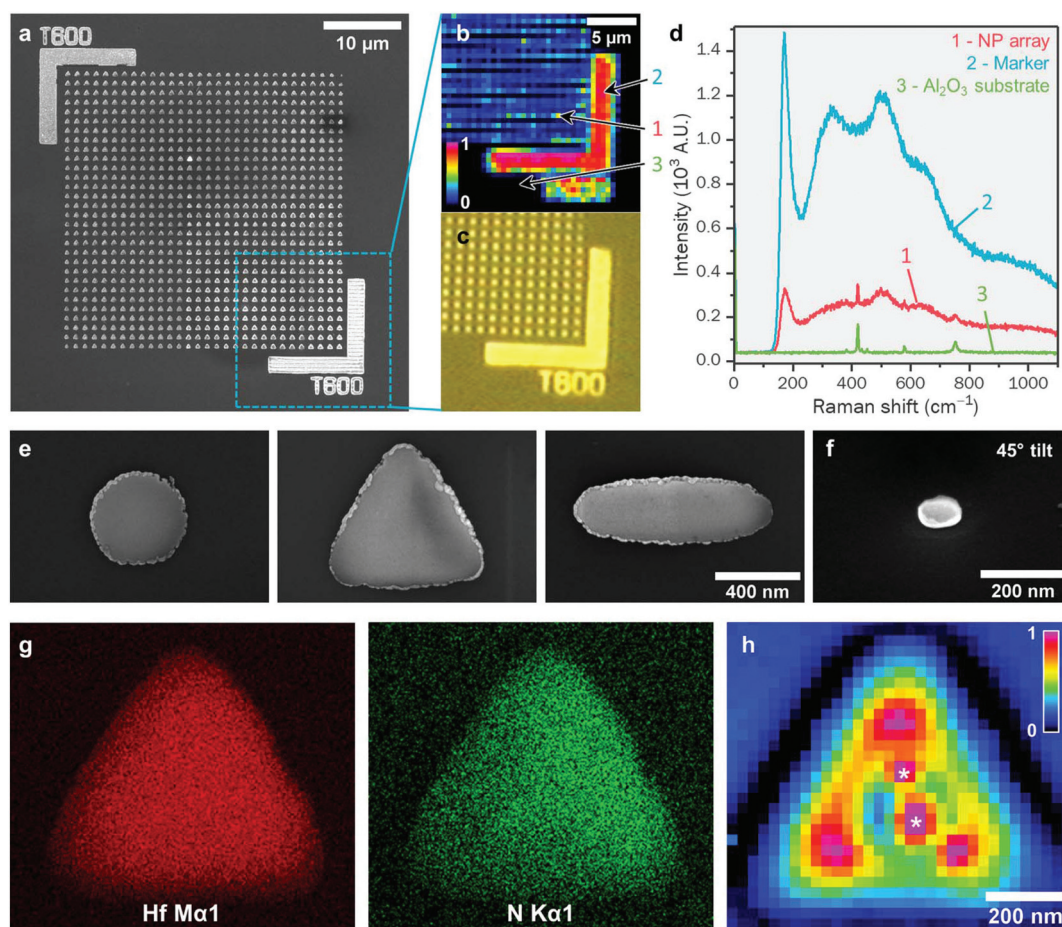


Fig. 3 Characterization of HfN nanoparticle arrays prepared by electron-beam lithography. (a) SEM image of a field of 25×25 HfN nanotriangles (600 nm equilateral size, 1.2 μm array pitch), including two HfN markers on two corners. (b) Normalized Raman spectroscopy map of the integrated spectral signal. (c) Bright field image of the same region, imaged through a 532 nm long-pass filter. (d) Raman spectra of the HfN nanoparticle array (red, #1), HfN marker (blue, #2), and the sapphire background (green, #3), locations indicated with arrows on panel (b). The transverse-acoustic phonon peak at 120 cm^{-1} is not visible due to the filter cutoff at $\sim 150\text{ cm}^{-1}$. (e) SEM images of a 300 nm disk, 600 nm equilateral triangle, and 800×150 nm ellipse. See also AFM in Fig. S20† (f) SEM image at 45° tilt of a 60 nm disk. The experimental diameter is 100 nm, indicating partial filling of the resist undercut with nitride material during sputter coating. (g) EDX map of Hf (red, left) and N (green, right) under 5 kV electron impact of a 600 nm equilateral triangle. (h) Normalized cathodoluminescence map at $\lambda = 550 \pm 50$ nm of a 600 nm HfN nanotriangle. Asterisks indicate incidental lithography artifacts, see SEM in Fig. S23†

resist walls due to the non-directionality of HfN sputter coating and the 35° angle between target and substrate, which is default in our sputter coater, thereby producing thin cylindrical structures that did not feature the Raman spectral fingerprint of HfN (Fig. S17†). We attribute this to the reaction of HfN sputtered particles with the oxygen and carbon-rich resist, leading to an undesired material combination.

We addressed these challenges by (1) adjusting the sample to face the sputter target perpendicularly, and (2) replacing the single-layer resist by a triple-layer stack of CSAR-62, germanium, and PMMA to engineer a plasma-etched undercut in the bottom layer (see ESI and Fig. S18†). Since the substrates were not heated during HfN deposition, the use of polymer resists posed no restrictions, which avoided the requirement for using hard-masks, *e.g.* Cr.¹⁹ The final step consisted of tape-stripping of persistently adhered HfN walls (Fig. S19†), leading to clean arrays with a diversity of nanodisks, rods, and triangles (Fig. 3a/e and Fig. S20†). Features down to 100 nm were successfully patterned with reasonable fidelity (Fig. 3f). The maximum height of the particle gradually decreased when approaching smaller structure dimensions (Fig. S21†), presumably because the patterned resist gap closes at the top during HfN deposition, thereby limiting further deposition on the substrate. EDX confirmed that these nanoparticles consisted of hafnium and nitrogen (Fig. 3g and Fig. S22†), and the Raman spectrum of the nanoparticles was identical to that of the thin film (Fig. 1g and 3d), together indicating that the nanoparticles consisted of high quality HfN. Thus, here it is demonstrated that relatively simple positive-tone resists and the sputter deposition of a refractory material are not fundamentally incompatible. We believe that our patterning methodology can be readily applied for other materials that rely on reactive sputter coating to reach high quality, *e.g.* the other metal nitrides (ZrN/TaN/MoN/WN *etc.*). Further upscaling could be achieved by combining the triple-layer sputter-coating strategy with, for instance, Substrate Conformal Nanoimprint Lithography (SCIL)⁴⁴ or Nanosphere Lithography (NSL).⁴⁵

The plasmonic resonances of the lithographically fabricated HfN structures were mapped using cathodoluminescence under 30 keV electron excitation (Fig. 3h and Fig. S23†). Since the deposited HfN material was confirmed to be of the same high quality as the thin films, we expected the existence of plasmon modes in these nanoparticles. Indeed, for 450 and 600 nm equilateral triangles the CL maximized near the three triangle tips throughout the visible spectrum, in a similar way as for the FIB-milled equivalents, which points towards observation of the same plasmon resonance. For a 700 × 150 nm ellipse the first-harmonic plasmon mode was observed with CL-maxima near the tips (Fig. S23†). For a 900 × 300 nm rectangle, this first-harmonic mode was better distinguishable on the longitudinal edges and a higher-harmonic mode was observed in the middle of the structure (Fig. S23†). Finally, for a 300 nm nanodisk the emission was more intense in the outer ring than in the center at short wavelengths (Fig. S23†), which reversed towards NIR wavelengths. We interpret the

outer ring mode as a higher order mode, similar to higher order modes observed for Au nanodisks,⁴⁶ while the center mode may correspond to the dipolar mode in the NIR.

For all these plasmon modes the CL-spectrum does not exhibit any distinguishable peaks in the observed region. Instead, in each case we observe the rise of emission intensity towards longer wavelengths, indicating that the main resonance is in the near-infrared. This mirrors our experimental data for the FIB-milled structures. We attribute the poor contrast of the CL map compared to that of the FIB-milled structures to the unequal height of the lithographically fabricated structures (Fig. S20†). Nonetheless, the similarity between CL modal maps for FIB-milled and EBL-prepared structures strongly suggests that the same plasmon modes are observed for both types of nanoparticles. Taken altogether our data identifies for the first time the existence of LSPR modes in lithographically fabricated HfN nanoparticles, which creates many opportunities to apply this advantageous material in a diversity of plasmonic applications.

Conclusions

In conclusion, crystalline HfN thin films were produced by reactive sputter coating for which XPS depth-profiling and RBS measurements confirmed 1 : 1 stoichiometry and high purity. The optical constants showed Drude-like metallic behavior above a screened bulk plasmon resonance of $\lambda = 370$ nm, while optical losses strongly increased above $\lambda = 700$ nm. A diverse set of nanorod and nanotriangles was produced either by FIB-milling from a thin film, or through positive-tone electron-beam lithography in combination with lift-off. For both fabrication methods, CL maps in the visible range show standing-wave plasmon resonances on the nanorods and localized resonances on the nanotriangles. First-harmonic resonances were located at NIR wavelengths, while higher-harmonics were observed in the visible range. Importantly, plasmon resonances in lithographically fabricated HfN nanoparticles were found to be very similar to those in FIB-milled particles, which represents an advance towards preparation of large-area devices for thermoplasmonics and photocatalysis. Overall, this work conceives many opportunities for further exploring HfN nanoparticles, which offer structural advantages over the classical noble metal nanostructures because of their high temperature stability and mechanical robustness.

Experimental section

General techniques

Samples were prepared in a cleanroom environment. Layer thicknesses were measured using a KLA-Tencor alpha-step 500 surface profiler. Atomic Force Microscopy (AFM) was performed on a Veeco Dimension 3100 AFM or Park NX10. E-beam lithography (EBL) was performed on a Raith e-LINE system, operating at 50 kV electron acceleration. Reactive Ion

Etching (RIE) was performed on an Oxford Plasmalab 80+ etcher. Scanning electron microscopy (SEM) was performed on a FEI Verios 460 with a typical acceleration beam voltage of 5 kV and 100 pA beam current, using the secondary electron mode, unless otherwise specified. Energy dispersive X-ray spectrometry (EDS) was performed with an Oxford Instruments device with a beam acceleration voltage of 5 kV and current of 1.2 nA. X-ray diffraction (XRD) was done with a Bruker D2 Phaser with Cu K α radiation ($\lambda = 1.5406 \text{ \AA}$). Instrumental broadening (0.09° FWHM) was determined using a corundum standard (Bruker AXS Korundprobe A26-b26-S). K α 2 peaks were stripped using Bruker DIFFRAC.SUITE software. Ellipsometry was performed on a Woollam variable angle spectrometric ellipsometer (VASE) and optical constants were retrieved using CompleteEASE software. Raman spectral maps were acquired using a WITec alpha300 S R confocal Raman microscope, operating with 50 mW 532 nm excitation and using a 532 nm long pass filter to collect Raman scattering. Rutherford backscattering spectroscopy (RBS) was performed at the Ion Beam Facility (IBF) at DIFFER (Eindhoven, The Netherlands), using a 2.0 MeV ^4He ion beam at a scatter angle of 163°. Data was analyzed using SIMNRA 7.01 software. X-ray photoelectron spectroscopy (XPS) was performed using a Kalpha setup from Thermo Fisher Scientific that is equipped with a detector at normal incidence. The composition of the top surface was studied in a vacuum environment of 1×10^{-8} mbar where monochromatic Al-K α radiation has been used to investigate the surface. For quantification XPS sensitivity factors from the Scofield library were used.⁴⁷ Erosion depth profiles were performed using 500 eV Ar ion bombardment at 45° angle of incidence. All data was processed using Origin 2017 software and images were processed using ImageJ 2.0 software.

Reactive sputter coating of HfN

HfN was deposited using a Flextura reactive sputter coating system (Polyteknik AS, Denmark) with a base pressure of 3×10^{-8} mbar. A pure Hf target was used, which was sputter cleaned for at least 2 minutes prior to deposition. The substrate holder was mounted at approximately 25 cm distance from the target under a 35° angle, and the substrate was rotated at 4 rpm during deposition unless otherwise specified. HfN was deposited using radio frequency (RF) magnetron sputtering at 150 W power at a pressure of 2×10^{-3} mbar in a mixture of 34.5 sccm Ar and 1.5 sccm N $_2$, unless otherwise specified. The coating rate was typically 8 nm min $^{-1}$. No active heating was used, because preliminary data indicated negligible influence of heating up to 500 °C on the optical properties of HfN thin film.

Focused ion beam milling

12 × 12 mm silicon (100) slides containing a 70 nm layer of HfN were loaded in a FEI Helios Nanolab 600 scanning electron microscope. A box of 4 × 4 × 0.3 μm (length × width × height) of HfN and Si material was milled away around a central nanoparticle using a Ga liquid metal ion source that operated at 30 kV acceleration voltage and a typical ion current of 28 pA.

E-beam lithography

12 × 12 mm silicon (100) or sapphire (c-plane 0001) slides were spin coated at 4000 rpm for 45 seconds (1000 rpm per s acceleration, closed bowl) with 100 μL PMMA A8 495 (MicroChem Corp., Westborough, MA, USA), and baked for 30 min at 180 °C to yield a hard-baked 500–550 nm resist layer. A home-built evaporator was used to deposit 20 nm germanium at a deposition pressure of 6×10^{-6} mbar and with a rate of 1 \AA s^{-1} . Then the slides were spin coated at 2000 rpm for 45 s (1000 rpm per s acceleration, closed bowl) with 60 μL 1:1 anisole:CSAR 62 (Allresist GmbH, AR-P 6200.09) and baked at 150 °C for 2 min to yield a 64 nm top resist layer. The resist was nanopatterned using EBL with an electron dose of 320 $\mu\text{C cm}^{-2}$ and a writing speed of 15 mm s $^{-1}$. The exposed nanostructures in the CSAR top-layer were developed through a sequential treatment with pentyl acetate (2.5 min), *ortho*-xylene (6 s), 9:1 v/v methylisobutylketone:isopropanol (15 s), and isopropanol (15 seconds), and were finally dried with nitrogen. The Ge layer was then etched for 1 min using RIE at 30 W forward power, 8 mTorr plasma pressure, and 12.5:2.5 sccm SF $_6$:N $_2$ gas flow. The PMMA bottom-layer was etched and undercut using RIE at 50 W forward power, 30 mTorr plasma pressure, and 25 sccm O $_2$ gas flow for 9 min. A 110 nm HfN layer was deposited by reactive sputter coating at room temperature at ~0–10° angle offset with respect to the sputter target and without sample rotation. The resist layers were lifted off by dipping the slides in acetone at 45 °C for 2 min followed by 10 min of sonication. Finally, the remaining resist fragments were stripped off by applying standard office tape, gently peeling it off, and rinsing the sample with acetone and isopropanol.

Cathodoluminescence

Cathodoluminescence experiments were performed inside a Thermo Fisher 650 Quanta field-emission gun scanning electron microscope. The applied acceleration potential is 30 kV and the current is 4.5 nA. The CL signal is collected and measured using a Delmic SPARC system equipped with a 2048 × 512 pixel back-illuminated CCD array (Andor Newton DU940P-BU) mounted on a Czerny-Turner spectrograph. The light is collected with an aluminium paraboloid mirror (1.47 π sr acceptance angle). The spectrograph contains a motorized entrance slit, a filter wheel with band-pass color filters, and a turret with a 300 lines per mm ruled grating, blazed for a free space wavelength $\lambda = 500 \text{ nm}$ and a flat Al mirror. We performed two kind of CL experiments. For CL spectroscopy, we closed the entrance slit to 200 μm and used the blazed grating in the spectrograph. The spectral data was corrected for the system response to give an output of emission probability (photons/nm/incident electron). The system response was obtained by measuring the transition radiation of an Al single-crystalline surface and comparing the spectrum with theory.⁴⁸ Background spectra, *i.e.*, without electron beam current, were subtracted from the data.

Conflicts of interest

The authors declare the following competing financial interests: A.P. is co-founder and co-owner of Delmic BV, a startup company that produces the cathodoluminescence system that was used in this work.

Acknowledgements

We thank Ruben Hamans, Matteo Parente, Rifat Kamarudheen, Gayatri Kumari, Andrea Baldi (DIFFER, Eindhoven, The Netherlands), Andrea Cordaro, Annemarie Berkhout, and Femius Koenderink (AMOLF, Amsterdam) for insightful discussions. We gratefully acknowledge Bob Drent, Andries Lof, Dimitry Lamers, Hans Zeijlemaker, and Johan Derks (AMOLF Nanolab Amsterdam) for technical assistance with clean room processes, sputter coating, and nanolithography. This work is part of the research program of the Foundation for Fundamental Research on Matter (FOM), which is financially supported by the Netherlands Organisation for Scientific Research (NWO). This project has received funding from the European Research Council (ERC) under the European Union's Horizon 2020 research and innovation programme (grant agreement no. 695343).

References

- 1 P. Patsalas, N. Kalfagiannis, S. Kassavetis, G. Abadias, D. V. Bellas, C. Lekka and E. Lidorikis, Conductive Nitrides: Growth Principles, Optical and Electronic Properties, and Their Perspectives in Photonics and Plasmonics, *Mater. Sci. Eng., R*, 2018, **123**, 1–55.
- 2 U. Guler, V. M. Shalaev and A. Boltasseva, Nanoparticle Plasmonics: Going Practical with Transition Metal Nitrides, *Mater. Today*, 2015, 227–237.
- 3 U. Guler, A. Boltasseva and V. M. Shalaev, Refractory Plasmonics, *Science*, 2014, **344**(6181), 263–264.
- 4 *Handbook of Chemistry and Physics*, ed. W. M. Haynes, CRC Press, 97th edn, 2017.
- 5 Y. Zhang, S. He, W. Guo, Y. Hu, J. Huang, J. R. Mulcahy and W. D. Wei, Surface-Plasmon-Driven Hot Electron Photochemistry, *Chem. Rev.*, 2018, **118**(6), 2927–2954.
- 6 M. L. Brongersma, N. J. Halas and P. Nordlander, Plasmon-Induced Hot Carrier Science and Technology, *Nat. Nanotechnol.*, 2015, **10**(1), 25–34.
- 7 Q. Wei, S. Wu and Y. Sun, Quantum-Sized Metal Catalysts for Hot-Electron-Driven Chemical Transformation, *Adv. Mater.*, 2018, **30**(48), 1–16.
- 8 S. Chung, X. Wen, S. Huang, N. Gupta, G. Conibeer, S. Shrestha, T. Harada and T. W. Kee, Nanosecond Long Excited State Lifetimes Observed in Hafnium Nitride, *Sol. Energy Mater. Sol. Cells*, 2017, **169**(September), 13–18.
- 9 S. Chung, S. Shrestha, X. Wen, Y. Feng, N. Gupta, H. Xia, P. Yu, J. Tang and G. Conibeer, Hafnium Nitride for Hot Carrier Solar Cells, *Sol. Energy Mater. Sol. Cells*, 2016, **144**, 781–786.
- 10 T. S. Ahmadi, S. L. Logunov and M. El-Sayed, a. Picosecond Dynamics of Colloidal Gold Nanoparticles, *J. Phys. Chem.*, 1996, **100**(20), 8053–8056.
- 11 S. L. Shinde, S. Ishii, T. D. Dao, R. P. Sugavaneshwar, T. Takei, K. K. Nanda and T. Nagao, Enhanced Solar Light Absorption and Photoelectrochemical Conversion Using TiN Nanoparticle-Incorporated C3N4-C Dot Sheets, *ACS Appl. Mater. Interfaces*, 2018, **10**(3), 2460–2468.
- 12 S. Ishii, S. L. Shinde, W. Jevasuwan, N. Fukata and T. Nagao, Hot Electron Excitation from Titanium Nitride Using Visible Light, *ACS Photonics*, 2016, **3**(9), 1552–1557.
- 13 W. He, K. Ai, C. Jiang, Y. Li, X. Song and L. Lu, Plasmonic Titanium Nitride Nanoparticles for in Vivo Photoacoustic Tomography Imaging and Photothermal Cancer Therapy, *Biomaterials*, 2017, **132**, 37–47.
- 14 S. Exarhos, A. Alvarez-Barragan, E. Aytan, A. A. Balandin and L. Mangolini, Plasmonic Core-Shell Zirconium Nitride-Silicon Oxynitride Nanoparticles, *ACS Energy Lett.*, 2018, **3**(10), 2349–2356.
- 15 U. Guler, D. Zemlyanov, J. Kim, Z. Wang, R. Chandrasekar, X. Meng, E. Stach, A. V. Kildishev, V. M. Shalaev and A. Boltasseva, Plasmonic Titanium Nitride Nanostructures via Nitridation of Nanopatterned Titanium Dioxide, *Adv. Opt. Mater.*, 2017, **5**(7), 1600717.
- 16 A. Naldoni, *et al.*, Broadband Hot-Electron Collection for Solar Water Splitting with Plasmonic Titanium Nitride, *Adv. Opt. Mater.*, 2017, **5**(15), 1601031.
- 17 R. Kamakura, S. Murai, K. Fujita and K. Tanaka, Enhanced Photoluminescence from Organic Dyes Coupled to Periodic Array of Zirconium Nitride Nanoparticles, *ACS Photonics*, 2018, **5**(8), 3057–3063.
- 18 S. Magdi, D. Ji, Q. Gan and M. A. Swillam, Broadband Absorption Enhancement in Organic Solar Cells Using Refractory Plasmonic Ceramics, *J. Nanophotonics*, 2017, **11**(1), 16001.
- 19 U. Guler, J. C. Ndukaife, G. V. Naik, A. G. A. Nnanna, A. V. Kildishev, V. M. Shalaev and A. Boltasseva, Local Heating with Lithographically Fabricated Plasmonic Titanium Nitride Nanoparticles, *Nano Lett.*, 2013, **13**(12), 6078–6083.
- 20 S. Murai, K. Fujita, Y. Daido, R. Yasuhara, R. Kamakura and K. Tanaka, Plasmonic Arrays of Titanium Nitride Nanoparticles Fabricated from Epitaxial Thin Films, *Opt. Express*, 2016, **24**(2), 1143.
- 21 J. A. Briggs, G. V. Naik, T. A. Petach, B. K. Baum, D. Goldhaber-Gordon and J. A. Dionne, Fully CMOS-Compatible Titanium Nitride Nanoantennas, *Appl. Phys. Lett.*, 2016, **108**(5), 051110.
- 22 R. A. Karaballi, G. Humagain, B. R. A. Fleischman and M. Dasog, Synthesis of Plasmonic Group-4 Nitride Nanocrystals by Solid-State Metathesis, *Angew. Chem., Int. Ed.*, 2019, **58**(10), 3147–3150.
- 23 S. A. Rasaki, B. Zhang, K. Anbalgam, T. Thomas and M. Yang, Synthesis and Application of Nano-Structured

- Metal Nitrides and Carbides: A Review, *Prog. Solid State Chem.*, 2018, **50**(May), 1–15.
- 24 S. Edlou and J. Simons, Optical and Electrical Properties of Reactively Sputtered TiN, ZrN, and HfN Thin Films, *Proc. SPIE*, 1994, **2262**, 96–106.
 - 25 M. Strømme, R. Karmhag and C. G. Ribbing, Optical Constants of Sputtered Hafnium Nitride Films. Intra- and Interband Contributions, *Opt. Mater.*, 1995, **4**(5), 629–639.
 - 26 C. G. Ribbing and A. Roos, Zirconium Nitride (ZrN) Hafnium Nitride (HfN), *Handb. Opt. Constants Solids*, 1997, pp. 351–369.
 - 27 R. Erwin, The Crystal Structures of Hf₃N₂ and Hf₄N₃, *Metall. Mater. Trans. B*, 1970, **1**(5), 1249–1252.
 - 28 M. Stoeck, H. S. Seo, I. Petrov and J. E. Greene, Effect of off Stoichiometry on Raman Scattering from Epitaxial and Polycrystalline HfN_x (0.85 × 1.50) Grown on MgO(001), *J. Appl. Phys.*, 2008, **104**(3), 033507.
 - 29 A. J. Perry and L. Schlapbach, An XPS Study of Hafnium Nitride Films, *Solid State Commun.*, 1985, **56**(10), 837–841.
 - 30 A. Arranz and C. Palacio, Core Level Spectra of Hafnium and Hafnium Nitride (HfN_{0.9}) by XPS, *Surf. Sci. Spectra*, 2006, **11**(1), 33–42.
 - 31 I.-S. Yu, H.-E. Cheng, C.-C. Chang, Y.-W. Lin, H.-T. Chen, Y.-C. Wang and Z.-P. Yang, Substrate-Insensitive Atomic Layer Deposition of Plasmonic Titanium Nitride Films, *Opt. Mater. Express*, 2017, **7**(3), 777.
 - 32 Q. N. Meng, M. Wen, C. Q. Qu, C. Q. Hu and W.T. Zheng, Preferred Orientation, Phase Transition and Hardness for Sputtered Zirconium Nitride Films Grown at Different Substrate Biases, *Surf. Coat. Technol.*, 2011, **205**(8–9), 2865–2870.
 - 33 T. Coenen and N. M. Haegel, Cathodoluminescence for the 21st Century: Learning More from Light, *Appl. Phys. Rev.*, 2017, **4**(3), 031103.
 - 34 F. J. García de Abajo, Optical Excitations in Electron Microscopy, *Rev. Mod. Phys.*, 2010, **82**(1), 209–275.
 - 35 A. Polman, M. Kociak and F. J. García de Abajo, Electron Beam Spectroscopy for Nanophotonics, *Nat. Mater.*, 2019, DOI: 10.1038/s41563-019-0409-1.
 - 36 O. Nicoletti, M. Wubs, N. A. Mortensen, W. Sigle, P. A. van Aken and P. A. Midgley, Surface Plasmon Modes of a Single Silver Nanorod: An Electron Energy Loss Study, *Opt. Express*, 2011, **19**(16), 15371.
 - 37 E. J. R. Vesseur, R. de Waele, M. Kuttge and A. Polman, Direct Observation of Plasmonic Modes in Au Nanowires Using High-Resolution Cathodoluminescence Spectroscopy, *Nano Lett.*, 2007, **7**(9), 2843–2846.
 - 38 E. S. Barnard, T. Coenen, E. J. R. Vesseur, A. Polman and M. L. Brongersma, Imaging the Hidden Modes of Ultrathin Plasmonic Strip Antennas by Cathodoluminescence, *Nano Lett.*, 2011, **11**(10), 4265–4269.
 - 39 A. Losquin, *et al.*, Unveiling Nanometer Scale Extinction and Scattering Phenomena through Combined Electron Energy Loss Spectroscopy and Cathodoluminescence Measurements, *Nano Lett.*, 2015, **15**(2), 1229–1237.
 - 40 L. Novotny, Effective Wavelength Scaling for Optical Antennas, *Phys. Rev. Lett.*, 2007, **98**(26), 1–4.
 - 41 S. Griffin, N. P. Montoni, G. Li, P. J. Straney, J. E. Millstone, D. J. Masiello and J. P. Camden, Imaging Energy Transfer in Pt-Decorated Au Nanoprisms via Electron Energy-Loss Spectroscopy, *J. Phys. Chem. Lett.*, 2016, **7**(19), 3825–3832.
 - 42 V. Myroshnychenko, N. Nishio, F. J. García De Abajo, J. Förstner and N. Yamamoto, Unveiling and Imaging Degenerate States in Plasmonic Nanoparticles with Nanometer Resolution, *ACS Nano*, 2018, **12**(8), 8436–8446.
 - 43 N. Kawasaki, S. Meuret, R. Weil, H. Lourenço-Martins, O. Stéphan and M. Kociak, Extinction and Scattering Properties of High-Order Surface Plasmon Modes in Silver Nanoparticles Probed by Combined Spatially Resolved Electron Energy Loss Spectroscopy and Cathodoluminescence, *ACS Photonics*, 2016, **3**(9), 1654–1661.
 - 44 M. A. Verschuuren, M. W. Knight, M. Megens and A. Polman, Nanoscale Spatial Limitations of Large-Area Substrate Conformal Imprint Lithography, *Nanotechnology*, 2019, **30**(34), 345301.
 - 45 C. L. Cheung, R. J. Nikolić, C. E. Reinhardt and T. F. Wang, Fabrication of Nanopillars by Nanosphere Lithography, *Nanotechnology*, 2006, **17**(5), 1339–1343.
 - 46 T. Coenen, F. Bernal Arango, A. Femius Koenderink and A. Polman, Directional Emission from a Single Plasmonic Scatterer, *Nat. Commun.*, 2014, **5**, 1–8.
 - 47 J. H. Scofield, Hartree-Slater Subshell Photoionization Cross-Sections at 1254 and 1487 EV, *J. Electron Spectrosc. Relat. Phenom.*, 1976, **8**(2), 129–137.
 - 48 B. J. M. Brenny, T. Coenen and A. Polman, Quantifying Coherent and Incoherent Cathodoluminescence in Semiconductors and Metals, *J. Appl. Phys.*, 2014, **115**(24), 244307.